Applied Catalysis A, General 644 (2022) 118834

Contents lists available at ScienceDirect

Applied Catalysis A, General

journal homepage: www.elsevier.com/locate/apcata

Influence of temperature during pyrolysis of Fe-alginate: Unraveling the pathway towards highly active Fe/C catalysts

Joakim Tafjord [a], Samuel K. Regli [a], Achim Iulian Dugulan [b], Magnus Rønning [a], Erling Rytter [a], Anders Holmen [a], Rune Myrstad [c], Jia Yang [a,*]

[a] Department of Chemical Engineering, Norwegian University of Science and Technology, Trondheim, Norway
[b] Fundamental Aspects of Materials and Energy Group, Delft University of Technology, Delft, the Netherlands
[c] Department of Process Technology, SINTEF Industry, Trondheim, Norway

ARTICLE INFO

Keywords:
Alginate
Pyrolysis
Iron
Carbon
Fischer-Tropsch synthesis

ABSTRACT

Transition metals supported on carbons play an important role in catalysis and energy storage. By pyrolysis of metal alginate, highly active catalysts for the Fischer-Tropsch synthesis (FTS) can be produced. However, the evolution of the carbon (alginate) and transition metal (Fe^{3+}) during pyrolysis remains largely unknown and was herein corroborated with several advanced in situ techniques. Initially, Fe^{3+} was reduced to Fe^{2+}, while bound to alginate. FeO nucleated above 300 °C, destabilizing the alginate functional groups. Increasing temperatures improved carbonization of the carbon support, which facilitated reduction of FeO to α-Fe at 630 °C. Catalysts were produced by pyrolysis between 400 and 700 °C, where the highest FTS activity (612 $\mu mol_{CO}\ g_{Fe}^{-1}\ s^{-1}$) was achieved for the sample pyrolyzed at low temperature. Lower metal loading, due to less decomposition of alginate, moderated sintering and yielded larger catalytic surface areas. The results provide valuable knowledge for rational design of metal-alginate-based materials.

1. Introduction

Solid carbon is imperative for numerous applications, and its diverse properties stem from the many allotropes, and various compounds and composites that may be formed from carbon precursors, e.g. diamond, graphite, carbon fibers, cokes, carbon black, activated carbon, and carbon aerogels [1]. Some of these may in turn be surface-modified with functional groups to provide new properties [2,3]. The natural abundance of carbon presents a vast array of precursors for production of both mundane and advanced materials, in which heat treatment is often a key step. Pyrolysis, a term typically used when organic materials are involved, is a thermal treatment in an inert atmosphere, to prevent combustion and favor decomposition of the carbon precursor [4]. For advanced materials, the interest lies in the formation of solid carbon products, termed char. The pyrolysis conditions, such as temperature, heating rate, and dwell duration, are key variables for controlling the amount of char relative to gases and liquids, i.e., degree of carbonization. Char formation and degree of graphitization are also highly dependent on the carbon precursor and how it is treated, e.g., molecular structure, porosity, and the presence of impurities like metals [5].

Porous carbons are utilized in several material applications, such as catalysis and energy storage, where transition metal nanoparticles are often confined within the carbon structure or pores [6]. Such materials have commonly been produced by impregnation or deposition-precipitation of pre-synthesized porous carbon structures, e.g. activated carbons, carbon nanofibers, and carbon nanotubes. Both methods are simple to execute, and impregnation grants control over metal loading but may result in poor metal dispersion at high metal loadings and pore blocking, which are often undesirable features [7]. A different approach is pyrolysis of carbon precursors with metal ions bound to their structure. A straightforward tactic is to use a polymer with appropriate functional groups that can bind metal ions, or advanced precursors such as metal-organic frameworks (MOFs), followed by pyrolysis [8,9].

A polymer with great potential for this application is alginate – a biopolymer extracted from brown seaweed. Alginate is comprised of two monomers: (1–4)-linked β-D-mannuronate (M), and its C-5 epimer, α-L-guluronate (G) (Fig. 1a). The spatial orientation and relative content of the two monomers will affect the interbonding and intrabonding properties in the presence of multivalent cations. The GG-diads have

* Correspondence to: Department of Chemical Engineering, Norwegian University of Science and Technology, 7491 Trondheim, Norway.
E-mail address: jia.yang@ntnu.no (J. Yang).

https://doi.org/10.1016/j.apcata.2022.118834
Received 30 May 2022; Received in revised form 12 August 2022; Accepted 15 August 2022
Available online 20 August 2022

historically been of importance for cross-linking alginate chains, proposed to form so-called "egg-box structures" (Fig. 1b) [10]. This enables alginate to serve as a scaffold to obtain atomic dispersion of metal cations between the macromolecular chains.

Studies of heating of metal alginates have focused on their flame-retardant properties [11–15] and the decomposition of alginate [16–18], typically only investigating the alginate or carbon by in situ characterization techniques such as thermogravimetric analysis (TGA) and Fourier-Transformed infrared spectroscopy (FTIR). The resulting materials after pyrolysis of metal alginates have been utilized for sorption of heavy metal ions and dyes from aqueous solutions [19–21], as anode materials [22,23], supercapacitors [24], electrocatalysts for oxygen reduction reaction (ORR) [25], and as catalysts for CO_2 hydrogenation [26] and NO_x abatement [27]. Specifications related to the M/G-content and monomer distribution in the alginate are rarely reported, and only alginate solutions with low concentrations have been utilized, less than 5 wt%. The pyrolysis temperature was typically in the range of 800–900 °C, resulting in well-carbonized carbon materials, but with extensive sintering of the metal particles, as there were no reports of particles below 10 nm. The metal species were usually only characterized after pyrolysis with ex situ techniques such as X-ray diffraction (XRD), Raman spectroscopy and transmission electron microscopy (TEM). The transition from metal-alginate to the final product remains unresolved but understanding the evolution of both carbon structure and metal species during pyrolysis is vital for tailoring material properties.

In our previous work, the green and Na-alginate was ion-exchanged with different transition metal ions, followed by pyrolysis at 500 °C to produce [28]. In particular, pyrolysis of Fe-alginate yielded desirable material properties for heterogeneous catalysis. Due to the promising nature of this material, herein, the evolution of Fe and C species during pyrolysis has been corroborated by both ex situ characterization and advanced in situ techniques such as XAS and Mössbauer spectroscopy. This was mainly performed to understand how the pyrolysis conditions affect the material properties, but catalysts were also prepared by performing pyrolysis in a range of suitable temperatures to see how these material properties affect their performance in high-temperature Fischer-Tropsch synthesis (FTS). In FTS, synthesis gas (syngas, CO and H_2) from biomass may react through a polymerization reaction to form green fuels and chemicals (hydrocarbons of varying lengths), and H_2O as a by-product. Additionally, Fe catalysts exhibit water-gas shift activity, a reaction where H_2O and CO form H_2 and CO_2. This enables Fe catalysts to use a syngas feed with low H_2/CO ratios, which is typically the result when syngas is produced from carbon-rich feedstocks such as biomass.

2. Experimental

2.1. Materials

Sodium alginate (Protanal LFR 5/60: G monad frequency (F_G) = 0.65–0.70, G diad frequency (F_{GG}) = 0.5–0.6, average length of G-blocks ($N_{G>1}$) = 11–20) was supplied by Dupont Nutrition Norge AS). Iron(III) nitrate nonahydrate (> 98 %) was supplied by Sigma-Aldrich, with impurities such as Cl^- (< 5 ppm), SO_4^{2-} (< 0.01 %), Ca^{2+} (< 0.01 %), Mg^{2+} (< 0.005 %), K^+(< 0.005 %), Na^+ (< 0.05 %). Ethanol (96 %) was supplied by VWR. Deionized water was produced by using a Milli-Q water purification system.

2.2. Synthesis

Na-alginate was dissolved in deionized water by a magnetic stirrer to form a 20 w/w% alginate/water solution. A solution of 0.1 M $Fe(NO_3)_3$-solution was prepared, with five times greater volume than that of the alginate. The Na-alginate solution was dripped into the $Fe(NO_3)_3$-solution, which formed alginate beads on contact, and was kept in solution for 24 h. The alginate beads were then washed by placing them in 200 mL deionized water for 5 min, discarding and replacing the water, repeated three times before they were immersed in ethanol-water solutions of increasing concentration over time to gradually transform the beads from hydrogels to alcogels. The initial ethanol concentration was 10 %, which was discarded and increased by 20 % every 10th min up to 90 %, before finally leaving the beads in a 96 % ethanol solution for 24 h. The beads were collected from the ethanol solution and dried at 80 °C overnight, followed by mortaring. Approximately 1 g of the dried powder was placed in a calcination reactor that allows gas to pass through the sample. Pyrolysis was performed by using a heating rate of 2° min^{-1} in 100 mL min^{-1} N_2 to the desired temperature, and dwelled at this temperature for a given time, as listed in Table 1. The samples were passivated in 1 % O_2 in Ar for 2 h at room temperature after pyrolysis, which is important due to the samples' pyrophoric nature.

2.3. Characterization

Powder XRD was recorded at ambient temperature with a Bruker D8

Table 1
Surface area (BET), pore size (BJH desorption), Fe particle size (TEM), and elemental loadings (ICP-MS) of the dried iron-alginate sample and the pyrolyzed samples.

Sample	Dwell time (h)	Surface area[a] (m^2/g)	Pore size[b] (nm)	Particle size[c] (nm)	Fe (w/w%)	Na[d] (w/w %)	S[d] (w/w%)
Fe-Alg	–	178	10.0	–	10.3	0.02	0.12
P400	8	250	13.5	2.8 ± 0.6	20.5	0.03	0.23
P500	8	350	12.6	3.0 ± 0.5	27.3	0.05	0.31
P600	8	481	13.2	4.8 ± 1.6	29.4	0.05	0.34
P700	1	552	11.5	7.1 ± 2.9	33.4	0.06	0.38

[a] BET specific surface area [b] BJH desorption average pore width [c] Number-average Fe particle size (± 95 confidence interval) from TEM images [d] For the pyrolyzed samples, the Na- and S-content is estimated from the dried sample.

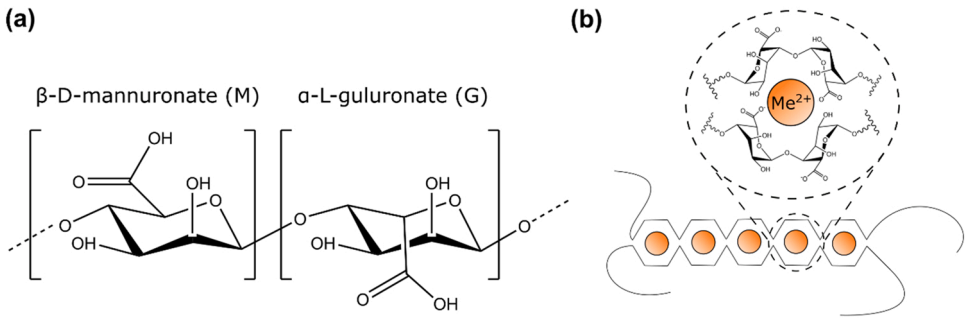

Fig. 1. a) The two monomers of alginate β-D-mannuronate (M), and its C-5 epimer α-L-guluronate (G), and b) the proposed "egg-box" model when GG-diad interacts with divalent cations.

A25 DaVinci X-ray Diffractometer using a Cu Kα-radiation (λ = 0.15432 nm) X-ray tube and LynxEye™ SuperSpeed detector. The samples were scanned in the range 2θ = 10–80° for 60 min, using a 0.2° divergence slit. The powder diffraction files (PDF) used as standards were α-Fe (7-9753), FeO (PDF 6-615), γ-Fe_3O_4 (9-2285), γ-Fe_2O_3 (21-3968), χ-Fe_5C_2 (36-1248), θ-Fe_3C (35-0772).

N_2 adsorption-desorption experiments were performed with a Micromeritics Tristar II 3000. Approximately 100 mg sample was degassed and evacuated for 24 h, at 353 K for the dried samples, and 473 K for the pyrolyzed samples. To determine the surface area, pore-volume, and pore diameters of the samples, the Brunauer-Emmett-Teller (BET) isotherm and Barrett-Joyner-Halenda (BJH) method (desorption) were used.

Thermogravimetric analysis (TGA) with differential scanning calorimetry (DSC) was performed with a Netzsch Jupiter 449 unit. The analysis was performed in pure argon (100 mL min^{-1}) or air (75 mL min^{-1}), with a ramp rate of 10 °C min^{-1}, heating from RT to 900 °C. A QMS 403 C Aëolos quadrupole mass spectrometer (MS) was used to analyze the effluent gases.

The elemental compositions of the iron alginate samples were measured by inductively coupled plasma mass spectrometry (ICP-MS). Between 10 and 30 mg of dried samples were mixed with 2 mL concentrated nitric acid (HNO_3) in perfluoroalkoxyalkane (PFA) vials. Further, the samples were digested in an UltraClave, heated to 245 °C, and pressurized to 50 bar. The resulting solutions were diluted to a total volume of 216.6 mL, then 16 mL of this solution was sent for analysis along. Three blank samples were used to correct the results. The elemental analysis was performed with a High Resolution Inductively Coupled Plasma ELEMENT 2 connected to a mass spectrometer.

The pyrolyzed samples were imaged by high-resolution (HR)-TEM. Experiments were performed with a JEOL JEM-2100 (LaB_6-filament, side-mounted Gatan 2k Orius CCD) and a JEOL JEM-2100F (200k Schottky field emission gun (0.7 eV energy spread) and bottom-mounted Gatan 2k Ultrascan CCD) both with Oxford X-Max 80 SDD energy-dispersive X-ray (EDX) (solid angle 0.24 sr) and scanning option with bright-field (BF) and high-angle annular dark-field (HAADF) detector. For sample preparation, the samples were suspended in isopropanol, then deposited on a Cu-grid with lacey carbon.

The D- and G-bands of the carbon in the pyrolyzed samples were analyzed with Raman spectroscopy. Experiments were performed with a Horiba ASD with a laser wavelength of 633 nm, employing a 600 g mm^{-1} grating, × 50 LWD objective, 15 acquisition, 3 accumulations, 25 % filter, and hole of 200. The powdered samples were placed on glass slides for analysis.

Transmission ^{57}Fe Mössbauer spectra were collected at different temperatures with conventional constant-acceleration or sinusoidal velocity spectrometers using a ^{57}Co(Rh) source. Velocity calibration was carried out using an α-Fe foil at room temperature. The source and the absorbing samples were kept at the same temperature during the measurements. The Mössbauer spectra were fitted using the Mosswinn 4.0 program [29]. The experiments were performed in a state-of-the-art high-pressure Mössbauer in-situ cell – recently developed at Reactor Institute Delft [30]. The high-pressure beryllium windows used in this cell contain 0.08 % Fe impurity whose spectral contribution was fitted and removed from the final spectra. The experiment at 700 °C was performed in a standard tubular reactor and the pyrolyzed sample was measured quasi in-situ (via glovebox transfer).

In situ XRD and X-ray absorption spectroscopy (XAS) was performed at the Swiss-Norwegian beamlines (BM31, European Synchrotron Radiation Facility (ESRF), France). The Fe-alginate sample was placed between two quartz wool plugs in a quartz capillary reactor (o.d. 1 mm), resulting in a bed length of 10 mm. The capillary was placed in an in situ cell, described elsewhere [31]. During the pyrolysis experiments, the capillary was purged with 10 N mL min^{-1} He, heating from RT (20 °C) to 700 °C at a rate of 2 °C min^{-1} at atmospheric pressure. The effluent gases that evolved were analyzed with an online MS. X-ray diffraction data were collected with a 2D plate detector (Mar-345) using monochromatic X-rays with a wavelength of 0.4975 Å. A lanthanum hexaboride (LaB_6) standard was used as a calibration reference. X-ray absorption near-edge spectroscopy (XANES) and extended X-ray absorption fine structure (EXAFS) were measured at the Fe K-edge, ranging from 7.05 to 8.2 keV, in transmission mode. The XAS data were analyzed using DLV Excurve and Feffit. A linear pre-edge was subtracted, and the data were normalized by the edge-jump. The background was subtracted to yield the data in χ(k), which was k^2-weighted before applying the Fourier-transform. EXAFS data were generally fitted in a k-range of 3.5–9.5 $Å^{-1}$, due to the deterioration of the signal at high temperatures, and an R-range of 1.0–3.8 $Å^{-1}$. For the amplitude reduction factor (S_0), metallic Fe was extracted from the metallic Fe foil measurement, and the Fe-alginate (RT) was extracted from $Fe(NO_3)_3$. Coordination number (*N*), energy shift (ΔE_0), scattering distance (R) and Debye-Waller factor ($2\sigma^2$) were refined for each scattering path.

The absorbances from the XANES measurements were placed in a matrix *A* with *m* rows (energy) and *n* columns (sample). The variance in the dataset was ranked by using singular-value decomposition (SVD), by the following equation:

$$A = U \times S + V$$

where *U* (*m x m*) is the left singular matrix, *S* is the singular-value matrix and V^T is the right singular matrix. The *S* matrix gives us the variance of each point in the dataset, for the initial evaluation of the number of pure components. Simple-to-use interactive self-modeling analysis (SIMPLISMA) was used to provide initial estimates for the pure components in the data set [32]. These estimates were then analyzed by multivariate curve resolution alternating least-square regression (MCR-ALS), to approximate the composition of components in a dataset with mixtures of components, using the equation [33]:

$$A = C \times S^T + \varepsilon$$

where *C* is the concentration of the relative concentration of the initial components contained in *S*, and ε is the error. The analysis assumes that the pure components have the lowest noise relative to the other spectra in the data. Constraints of non-negativity and normalization were applied, to obtain concentrations summing up to 100 %.

Diffuse reflectance infrared Fourier Transform spectroscopy (DRIFTS) measurements of all samples were conducted in a Thermo Scientific Nicolet iS50 FT-IR Spectrometer with a Harrick Praying Mantis™ high temperature in situ cell, flushed with 30 mL min^{-1} Ar. A spectral range of 4000–600 cm^{-1} was used, with a resolution of 4 cm^{-1} and 32 scans being averaged for each spectrum. The samples were heated from RT to 500 °C at a rate of 5 °C min^{-1}, halting the heating at every 50 °C to perform measurements.

2.4. Catalytic tests

The FTS experiments were performed in a 10 mm i.d. tubular stainless-steel fixed bed reactor at 340 °C, 20 bar, and $H_2/CO = 1.0$. The catalysts (0.10 g, 90–250 μm sieve fraction) were diluted and mixed with inert SiC (10 g, 90–250 μm sieve fraction) to minimize temperature gradients. To keep the catalyst bed fixed, the mixture was loaded into the reactor between two plugs of quartz wool. The reactor was mounted between two aluminum blocks in an electrical furnace to further improve heat distribution. The catalysts were reduced in H_2 (100 N mL min^{-1}) at 3 bars with a heating rate of 2° min^{-1} to 400 °C, with a dwell time of 3 h. Then the reactor was cooled to 330 °C and pressurized to 20 bar with 56,100 N mL g^{-1} h^{-1} H_2. Syngas (48.5 % CO, 48.5 H_2, 3 % N_2) were then introduced in steps, replacing 25 % of the H_2 flow every 5th minute, keeping the gas-velocity constant. The product stream was passed through a hot trap (90 °C) and a cold trap (25 °C) to collect condensable FT products, i.e., wax, light hydrocarbons, water, and oxygenates. The gas-phase products were analyzed with an Agilent

Technologies 6890N gas chromatograph (GC) equipped with a stainless steel Carbosieve S-II and an HP-plot Al_2O_3 column with a thermal conductivity detector (TCD) and flame-ionization detector (FID). The 3 vol % N_2 in the syngas mixture was used as an internal standard for the GC.

The molar flows of H_2O and H_2 were estimated by using oxygen and hydrogen mass balances, where oxygenate formation was disregarded. The WGS equilibrium constant (K_{eq}) was calculated by $K_{eq} = 10^{((-2.4198)+(0.0003855*(T)+(2180.6/T)))}$, and was compared to the WGS quotient (Q_{WGS}) based on the fraction of products and reactants.

3. Results

The results are divided into two sections. First, ex situ characterization after pyrolysis of Fe-alginate at 400, 500, 600, and 700 °C will be regarded. These materials were also tested for FTS, to understand how the resulting material characteristics affect the catalytic performance. Second, in situ pyrolysis experiments were investigated to elucidate the evolution of both iron and carbon species.

3.1. Ex situ characterization and Fischer-Tropsch synthesis

One batch of Fe-alginate was synthesized and split into four portions that were subjected to pyrolysis at different temperatures. The samples pyrolyzed at 400, 500, and 600 °C used a dwell duration of 8 h, whereas 1 h was selected for the 700 °C treatment to limit the extent of sintering.

The porosity inherent in Fe-alginate can be attributed to the interconnection of alginate macromolecules, which is facilitated by ion-exchanged Fe^{3+}. The measured BET (Brauner-Emmett-Teller) specific surface area of Fe-alginate was 178 $m^2\ g^{-1}$, with pores primarily in the mesopore size range. After pyrolysis, a significant increase in BET surface area was observed for every step increase in temperature (Table 1, Fig. S1). In all cases, the pyrolysis treatment yielded pore sizes larger than for the Fe-alginate, and the total pore volume was also observed to increase with increasing temperature (Fig. S2). The observed changes in porosity can be attributed to both advancement of polymer decomposition and the development of by-products, which can lead to both expansion and formation of new pores.

The dried Fe-alginate sample contained 10.3 wt% Fe, dictated by the amount of Fe^{3+} that can be crosslinked within the alginate gel. The decomposition of alginate constituents innately increased the Fe loading with increasing pyrolysis temperature. Relatively to Fe-alginate, the Fe loading doubled for P400, while for the other samples, roughly a threefold increase was achieved (Table 1). This indicates that a significant decomposition of alginate occurred above 400 °C.

The powder X-ray diffractograms of the pyrolyzed samples, cooled to ambient temperature and exposed to air, are presented in Fig. 2. Broad and indistinct diffraction peaks were discerned for P400, which may originate from magnetite (γ-Fe_3O_4) or maghemite (γ-Fe_2O_3). These iron oxides are isostructural, the only difference is that magnetite has 2/3 Fe^{3+} and 1/3 Fe^{2+}, whereas maghemite contains Fe^{3+} ions exclusively. This grants two highly similar diffraction patterns that are difficult to differentiate with the low-range ordering present in the present samples. Similar diffraction patterns were also present in P500 and P600, more defined yet still broad, indicative of increasing ordering due to particle growth. With increasing pyrolysis temperature, diffractions corresponding to ferrite (α-Fe) emerged, first for P500, then with an increase in intensity for P600, while the oxide diffraction diminished. If present, oxide phases were not discernible for P700, but the Fe species in the sample had reduced drastically and partially carburized into cementite. The most intense α-Fe diffraction peak, Fe(110), at $2\theta = 45°$ overlaps with θ-Fe_3C(211) and (103), but the Fe(200) diffraction peak at $2\theta = 65°$ confirmed the presence of α-Fe.

Images captured with TEM (Fig. 3) showed amorphous carbon structures containing densely packed spherical Fe particles. As the average Fe particle size for P400 and P500 was relatively similar (Table 1), the increase in pyrolysis temperature from 400 to 500 °C did not lead to significant particle growth. The analysis of crystallinity and lattice fringes was not straightforward due to the size of the Fe particles. Larger particles were observed for P600, where some iron particles were completely reduced (Fe/Fe_xC_y), and some had a reduced core and a surrounding oxide shell, supported by an EDS line scan (Fig. S3). The EDS scan revealed a higher S density on the Fe particles, while Na was distributed more evenly in the sample, which is sensible, as S originated from the Fe precursor and the Na from the alginate. As the density difference of Fe atoms in iron oxides and metallic structure change the extent of electron transmission, darker areas indicate reduced Fe. Even larger particles and a broader particle size distribution were observed for P700 (Fig. S4). Similar Fe particle structures to P600 were seen for P700, but darker particles were also observed, indicative of more reduced Fe.

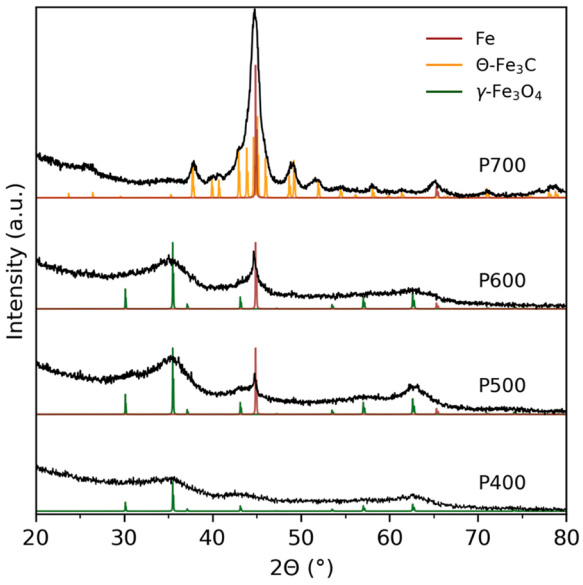

Fig. 2. Powder XRD patterns of Fe-Alginate pyrolyzed at 400 °C for 8 h (P400), 500 °C for 8 h (P500), 600 °C for 8 h (P600), and 700 °C for 1 h (P700) after cooling and being subjected to passivation in 1 % O_2. The red star marks the diffraction peak of α-Fe that does not overlap with θ-Fe_3C.

The D-band (1350 cm^{-1}) and G-band (1580 cm^{-1}) region were measured with Raman spectroscopy, to investigate the bonding modes present in the carbon support. The relative intensity of the bands (I_D/I_G) is commonly used to quantify defects in graphitic and diamond-like structures, but the pyrolysis temperatures employed here are not likely sufficient to form graphite. Thus, the assignment of D- and G-band could be misleading. A study on pyrolysis of saccharose showed that the I_D/I_G ratio increased up to 2000 °C [34]. The I_D/I_G ratio of the pyrolyzed samples (Fig. 4) increased with increasing temperature, similar to the aforementioned study, and also a blue-shift of the D-band and a red-shift of the G-band. An increasing I_D/I_G ratio in this temperature regime has been associated with increasing size of the structural carbon units [35]. The carbon material appears to be amorphous, but the increased ordering of the carbon structure was observed between 400–500 °C, and 600–700 °C.

The samples were reduced in H_2 at 400 °C for 3 h before being tested as catalysts at high-temperature FTS conditions, where a high initial CO conversion level was observed for all samples (Fig. 5a). Because identical sample amounts were used, the samples with higher Fe content achieved a higher conversion level. However, the activities in terms of iron-time yield ($mol_{CO}\ g_{Fe}^{-1}\ h^{-1}$) showed an inversely proportional relation to the pyrolysis temperature (Fig. 5b), where P400, P500, and P600 obtained similar activity profiles and the deactivation mainly occurred during the first 40 h on stream. Before reaction, P700 was the only sample containing θ-Fe_3C, and the induction period experienced by

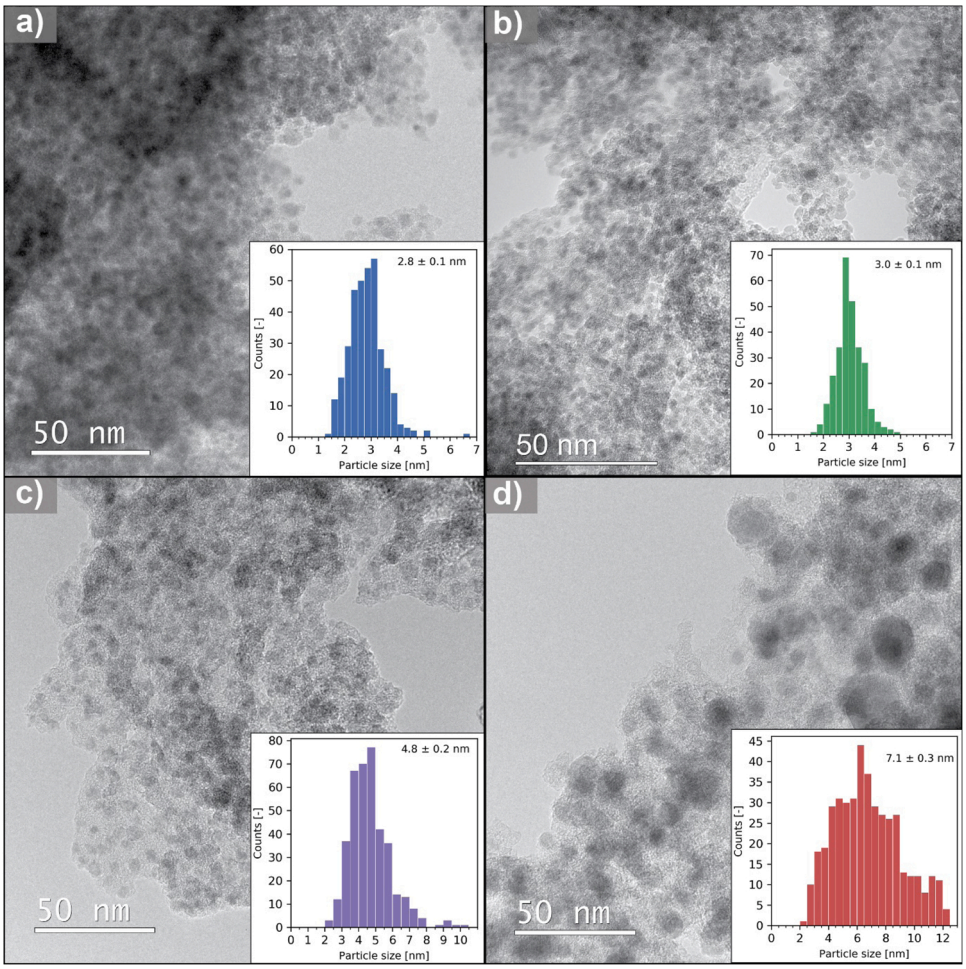

Fig. 3. TEM bright-field images of a) P400 b) P500 c) P600 and d) P700 with a scale bar in the left corner of each image, accompanied by a particle size distribution where the number-average particle size (± 95 % confidence interval) is also displayed.

this catalyst may be related to a slower interconversion of θ-Fe_3C to χ-Fe_5C_2. As both FTS and WGS are highly exothermic, the high activity of P400 resulted in higher temperature (Fig. S12), which in turn increases the activity further. The oven temperature was unchanged during the first 100 h of stream due to the high heat of inertia in our system and to observe the deactivation profile. To obtain comparable data, the temperature was adjusted to 340 °C after 100 h, as reported in Table 2.

Shorter hydrocarbons were produced by P400 and P500, compared to P600 and P700, but the C_2-C_4 olefins and paraffins selectivities were comparable for all samples. The changes in selectivity during reaction (Fig. S8), show similar results as discussed above, but P700 differs from the others by not stabilizing after 40 h on stream. All samples obtained the same CO_2 selectivity, which also implies that the WGS activity is comparable, as the amount of CO_2 is directly related to the former.At no point did the catalysts reach WGS equilibrium (Fig. S10).

For comparison, Table 2 contains FTS performance data for relevant carbon-supported catalysts from literature. The samples in the current work have fair activity compared to the referenced works, but they do not have particularly specific selectivity. Compared to the previous work on this type of catalyst (Fe/15C [28]), a higher activity and olefin selectivity was reported due to higher Na and S content from the catalyst synthesis. Sodium and sulfur were not added to any of these catalysts by intention, but a much higher olefin selectivity could be achieved by optimizing the promoter amount, akin to the iron catalyst support on graphene oxide and promoted with potassium (Fe/K1-rGO [36]). Optimization of the catalysts for FTS is beyond the scope of this work.

The diffractograms of the spent P400, P500 and P600 were similar, containing broad diffractions of χ-Fe_5C_2 and γ-Fe_2O_3, while P700 obtained more defined χ-Fe_5C_2 diffractions and a less prominent oxide phase (Fig. S7). At high-temperature FT conditions, χ-Fe_5C_2 is considered the active phase and is also the thermodynamically favored iron carbide.

The measured particle size from TEM images of the spent samples (Fig. S6) revealed a relatively similar number-average particle size (± 95 % confidence interval), with sizes of 12.6 ± 0.3 nm (P400), 15.2 ± 0.5 nm (P500), 15.1 ± 0.3 nm (P600) and 15.6 ± 0.4 nm (P700). The exception was P400, which experienced less sintering than the other sample, likely due to lower metal loading. As the core is much darker than the surrounding shell, there is an indication that the spent particles had an α-Fe or χ-Fe_5C_2 core and an outer layer comprised of iron oxide.

Mössbauer spectroscopy on spent samples that had been exposed to air revealed that the amount of χ-Fe_5C_2 increased from 12 % to 15 % for P400, P500, and P600, up to 38 % in P700, while all samples also contained 6–8 % ϵ'-$Fe_{2.2}C$ (Table S3). Deducing the extent of carburization during reaction from the contents of samples exposed to air is questionable, however, it seems reasonable that P700 achieved a greater extent of carburization. Before reduction in H_2 and introduction of syngas in FTS, P700contained partially reduced and carburized particles, as seen from XRD (Fig. 2) and Mössbauer (Table S2), which when activated yielded more χ-Fe_5C_2 than the other treatments after over 100 h on stream. No apparent catalytic activity benefit was observed from the increased content of χ-Fe_5C_2. The oxide contributions originated from γ-Fe_2O_3, but with various particle sizes. For P700, only very

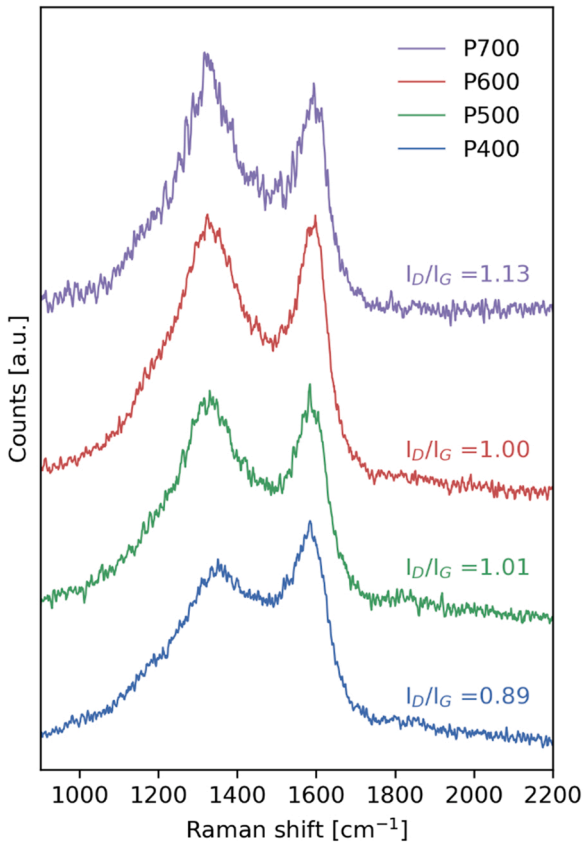

Fig. 4. The D- and G-band region of the normalized Raman spectra for the pyrolyzed samples, where the calculated intensity ratio of the two bands (I_D/I_G) are also displayed.

small and superparamagnetic (SPM) γ-Fe_2O_3 was observed, while for the other samples, intermediately sized γ-Fe_2O_3 was observed in addition.

An in situ Mössbauer experiment of the P500 sample after reduction and 20 h of FTS, showed that the catalyst consisted of 18 % χ-Fe_5C_2 and 82 % $Fe_{1-x}O$. The fitting parameters show that a relatively crystalline χ-Fe_5C_2 phase was formed, while the oxide phase was relatively disordered. After the experiments, the sample was exposed to air and measured again, where the sample contained only 8% χ-Fe_5C_2 and the remainder Fe^{3+}, due to oxidation (Table S2). The linewidth of χ-Fe_5C_2 increased significantly upon oxidation after reaction, indicating that the crystalline ordering decreased.

3.2. *In situ pyrolysis measurements*

The mass-loss and the accompanying effluent gases from the pyrolysis of the Fe-alginate were investigated using TGA-DSC coupled with MS. The sample was heated from RT to 900 °C in Ar at a rate of 10 °C min^{-1} (Fig. 6). The decomposition was divided into four different segments, where the first segment (I) involved dehydration (H_2O; $m/z = 18$) only, with an endothermic DSC signal. This process peaked between 100 and 120 °C, and the total dehydration yielded a mass-loss of 10 %. The second segment (II) took place between 160 and 350 °C, with the largest mass loss (50 %) throughout the entire experiment, the main effluent gases being H_2O and CO_2 ($m/z = 40$). This was followed by the third segment (III) between 350 and 550 °C, where a minor decomposition of 11 % mass loss occurred, with more CO_2 than H_2O evolving, compared to the previous segment. In the final segment, another mass loss of 11 % was observed, which was assigned to the reduction of the iron oxide, an endothermic process. The mass loss can be attributed to the carbon acting as a reductant, resulting in the release of both CO ($m/z = 28$) and CO_2. A study of the pyrolysis of Fe^{2+}-biopolymers (gelatin, chitosan, and alginate) demonstrated that a reduction of FeO to α-Fe or θ-Fe_3C was observed around 650 °C [39].

Mössbauer measurements were conducted after Fe-alginate was subjected to different heat treatments in Ar (Fig. 7, Table S1, Fig. S13) and subsequently cooled to 120 K (300 K for samples subjected to air after treatment). The untreated Fe-Alginate contained 90 % Fe^{3+} and 10 % Fe^{2+}, which was almost unchanged after heating the sample to 100 °C. At 200 °C, Fe^{2+} was almost exclusively observed, which was also the case at 300 °C, but small amounts of superparamagnetic (SPM) α-Fe could be fitted. For very small particle sizes α-Fe becomes SPM, when about half of their atoms are located at the surface, resulting in a nanoparticle that acts as a single magnetic domain. The quadrupole splitting (QS) of Fe^{2+} reduced as the temperature increased from 100 °C to 200 °C, implying higher charge symmetry at a higher temperature due to the removal of H_2O ligands during drying.

After treatment at 400 °C and a dwell time of 8 h (P400), the fraction of α-Fe (SPM) increased to 25 %, while the remainder consisted of Fe^{2+}. Two different Fe^{2+} species were observed, where one was fitted as $Fe_{1-x}O$ (6 %) as it has a hyperfine field and a QS close to zero. The remainder (69 %) has a very different QS (1.42 mm s^{-1}) than the

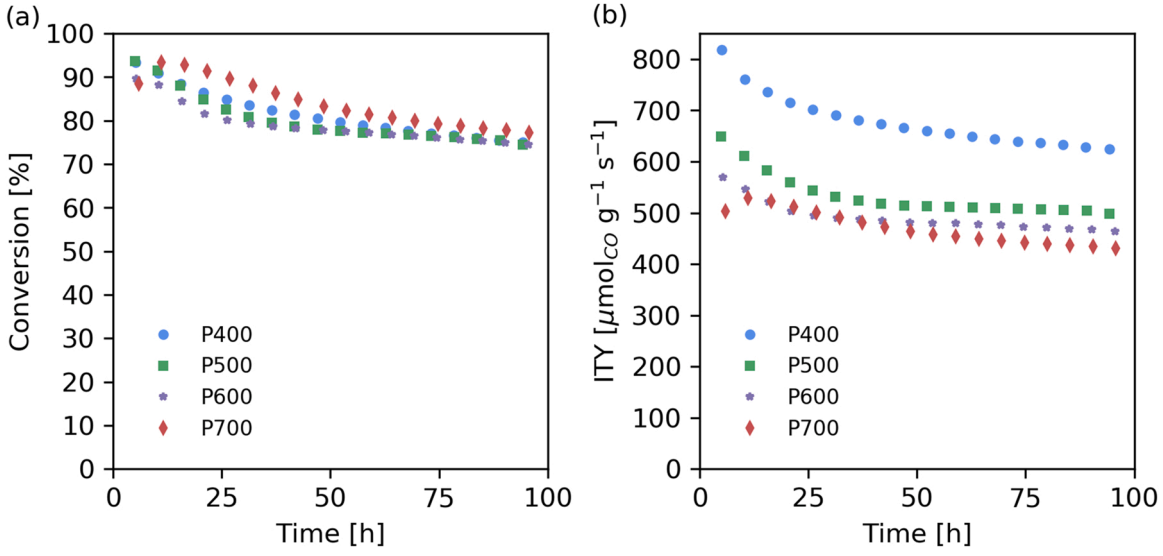

Fig. 5. The (a) CO conversion profile and (b) activity in ITY (iron-time yield) of the pyrolyzed Fe-alginate samples over the initial 100 h on stream.

Table 2
The catalytic activity (iron-time yield (ITY)) and product selectivity for the Fischer-Tropsch synthesis at T = 340 °C, P = 20 bar, H_2/CO = 1.0 after a specified time-on-stream (TOS) for the catalyst in this work, while other parameters in the referenced works are indicated by footnotes.

Catalyst	TOS (h)	GHSV h^{-1}	X_{CO} (%)	ITY ($\mu mol_{CO}\ g_{Fe}^{-1}\ s^{-1}$)	CO_2 (%)	Product selectivity (%C, CO_2-free)			
						CH_4 (%)	C_2-C_4 olefins (%)	C_2-C_4 paraffin (%)	C_{5+} (%)
P400	110	19,000	76	612	46	26	25	25	24
P500	111	19,000	80	530	46	26	23	27	24
P600	128	19,000	77	479	46	20	24	24	32
P700	118	19,000	83	461	46	21	23	23	33
Fe/15C [28]	90	34,000	83	885	46	17	29	15	39
Fe-MIL-88BNH$_2$/C [37][a]	30	36,000	82	320	43	15	13	21	51
Fe/K1-rGO [36]	24	72,000[b]	58–64	646	49–52	26	62	8	4
Fe/G-2g [38]	135	8000[c]	92	324	34	20	13	17	50

[a] Reaction temperature 300 °C [b] Space velocity reported in $mL_{syngas}\ g^{-1}\ h^{-1}$, while no specific X_{CO} or S_{CO2} was given, only a range for the tested catalysts [c] H_2/CO ratio = 2.0.

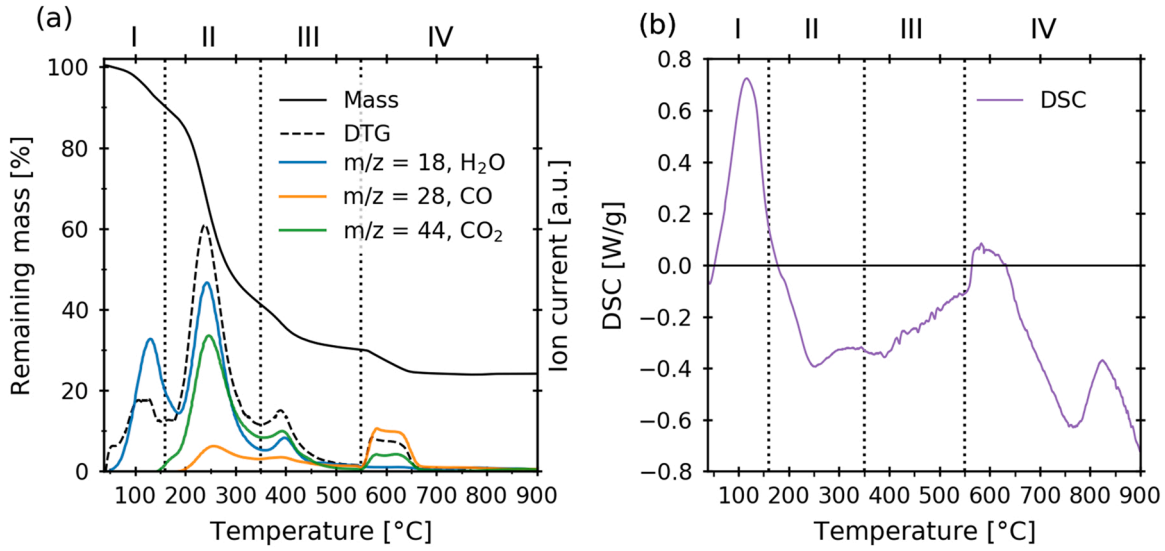

Fig. 6. a) The mass-loss and differential thermogravimetric (DTG) profile from TGA and MS data of the effluent gases and b) DSC-signal during the pyrolysis process of Fe-Alginate, divided into four mass-loss regions.

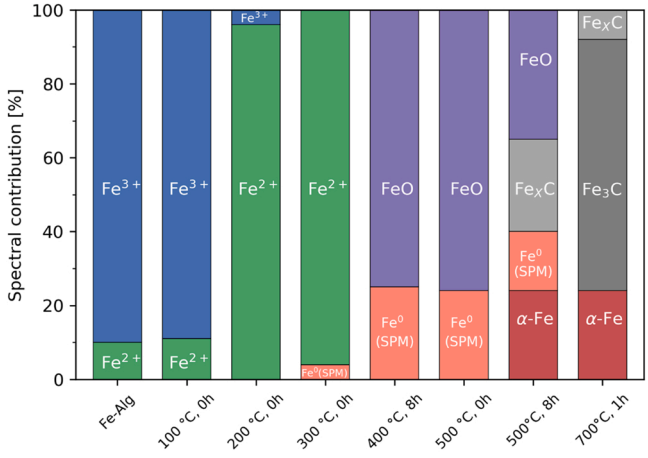

Fig. 7. The spectral contribution of identified species from fitted Mössbauer spectra after different pyrolysis treatments of Fe-alginate. SPM = superparamagnetic.

measurement at 300 °C (2.54 mm s^{-1}), and due to having no hyperfine field, it was assigned to very small particles of $Fe_{1-x}O$ that are super-paramagnetic (Table S1), adding up to a total of 75 % $Fe_{1-x}O$. Concerning this assignment of $Fe_{1-x}O$, this entails that the Fe^{2+} species with high QS observed at 200 °C (2.72 mm s^{-1}) and 300 °C are not $Fe_{1-x}O$, and the low charge symmetry implies that these are Fe^{2+} ions still bound to alginate.

The heat treatment at 500 °C with no dwell time yielded the same composition as for 400 °C for 8 h, but with species having smaller line widths, which could be due to higher crystallinity as an effect of higher temperature. However, dwelling at 500 °C for 8 h (P500) halved the number of Fe^{2+} (35%), and in addition to the SPM α-Fe (16 %), there was also SPM Fe_xC (25 %) and α-Fe (24 %). The formation of the latter indicates that an increase in temperature has led to some particle growth, as some α-Fe has lost its SPM properties. When this sample was cooled down and exposed to air, it was almost completely oxidized (96 % Fe^{3+}), containing small amounts of α-Fe (4 %) (Table S2). A sample was also measured after treatment at 700 °C for 1 h (P700), which yielded large quantities of θ-Fe_3C (68 %), some α-Fe (24 %), and small amounts of SPM Fe_xC (4 %) – the sample is completely reduced. Upon exposure to air, the sample was partially oxidized to Fe^{3+} (43 %), but the θ-Fe_3C (51 %) appeared to be difficult to re-oxidize.

The synchrotron experiment was performed by heating Fe-alginate from RT to 700 °C, while alternately recording XRD and XAS (Fig. 8, Fig. S16), with an experimental objective to elucidate the fate of the Fe species during pyrolysis. Initially, the dried Fe-alginate sample was XRD-amorphous – the broad diffraction peak around 21° originating from the quartz capillary, but also overlaps with alginate (002) [40]. At

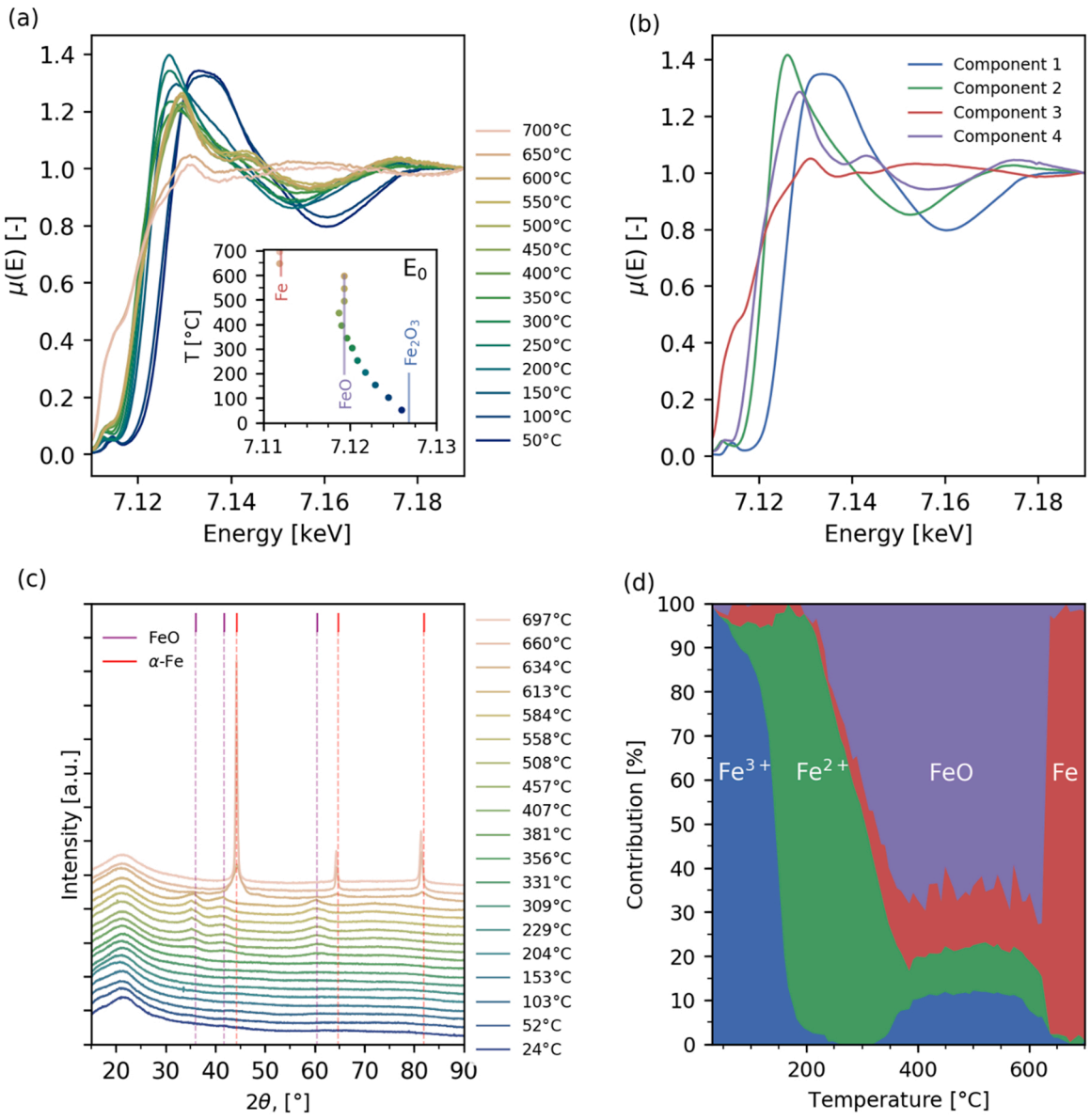

Fig. 8. In situ measurements of heating Fe-alginate in He from RT to 700 °C at a rate of 5 °C min^{-1}, a) normalized XANES for every 50 °C, with E_0 (maximum derivative) value in the indented plot b) the four MCR-ALS resolved pure components from 189 XANES measurements, c) XRD in situ measurements with indicated standards (FeO + Fe) d) the estimated concentration of MCR components in the acquired XANES data.

380 °C, very low-intensity diffraction peaks corresponding to FeO appeared, which increased in intensity with increasing temperature, indicating growth of the FeO particles. At 634 °C, FeO diffractions were promptly transformed into α-Fe and were accompanied by the release of CO – a stable signal until this point – and some CO_2 (Fig S14). At the next measurement (660 °C), sharp α-Fe diffractions were observed, indicating a rapid reduction and particle growth.

The initial XANES measurements exhibited a high absorption edge threshold energy (E_0, maximum of the derivative signal), indicative of Fe^{3+} – the same species introduced into the alginate matrix in the material synthesis. At 150 °C, E_0 was lowered, implying a reduction of Fe^{3+} to Fe^{2+}, accompanied by a shift of the pre-edge to lower energy. Approaching 350 °C, E_0 did not change significantly, but the spectra developed more characteristic features. The pre-edge also gained a wide feature towards the main edge, which is characteristic of FeO but may also have a contribution from broad features of the α-Fe edge. The next significant change was observed at 630 °C, where the spectra rapidly transformed to features that are distinct for α-Fe.

A total of 189 XANES spectra were measured over the temperature range, and MCR in conjunction with SIMPLISMA and SVD was utilized to estimate compounds that are not among the measured standards, and their concentration. Many pure components may be obtained, but only those that can account for a significant degree of variance, have meaningful spectra, and are significantly different from the other components, were used. This evaluation resulted in four calculated components, which are shown in Fig. 8(b) along with the concentration of these components over the temperature range (Fig. 8(d)) The pure components were matched with measured standards, where component 1 had an edge position similar to α-Fe_2O_3 and $Fe(NO_3)_3$, however, the spectrum was relatively featureless compared to both of these, and was assigned as Fe^{3+} bound to alginate. Components 2 and 4 are somewhat similar in terms of edge position, but component 4 has features that are very close to FeO and were assigned accordingly. Component 2 contained less prominent features, similar to component 1, and had a more defined pre-edge that was shifted towards lower energies, and is therefore likely a Fe^{2+} species, as it does not resemble any spectrum among

the measured standards. Component 3 has features matching with the Fe-foil and was assigned to α-Fe. Including more components than the four chosen here, yielded several variations of component 3 (α-Fe), where some may be linked to iron carbides. The concentration plot serves to give an estimate of the contributions of the selected components during the pyrolysis experiments. Some contributions, like α-Fe at the beginning and Fe^{3+} species between 400 °C and 600 °C, are not realistic but they provide the best fit given the limited set of components.

An in situ DRIFTS experiment was performed to investigate the pyrolysis temperature's effect on the alginate structure. The measurement obtained at RT (Fig. 9(a)), shows the bands present in Fe-alginate, which were; the broad band ranging from ~3000–3600 cm^{-1} (O-H stretching mode, $\nu(O\text{-}H)_s$); a weak signal located at 2938 cm^{-1} (aliphatic C-H stretching mode, $\nu(C\text{-}H)_s$); the intense peaks at 1629 cm^{-1} (antisymmetric COO stretching mode, $\nu(COO)_{asym}$) and 1429 cm^{-1} (symmetric COO stretching mode $\nu(COO)_{sym}$); the weak band at 1236 cm^{-1} (C-C-H and O-C-H deformation, δ(CCH) and δ(OCH)); the intense bands between 1133 and 1109 (C-O stretching vibrations of the pyranose rings $\nu(C\text{-}O)_s$); and the band at 1054 (C-O or C-C stretching, $\nu(C\text{-}O)_s$ and $\nu(C\text{-}C)_s$). The band at 1749 cm^{-1} was not observed for Na-alginate nor when gelated with divalent cations and does not appear to match with a carboxylic acid, and we have previously proposed that it might be related to an ester [41].

The Fe-alginate was heated from RT to 500 °C in He, measuring DRIFTS spectra every 50 °C. The absorbance was calculated by using the

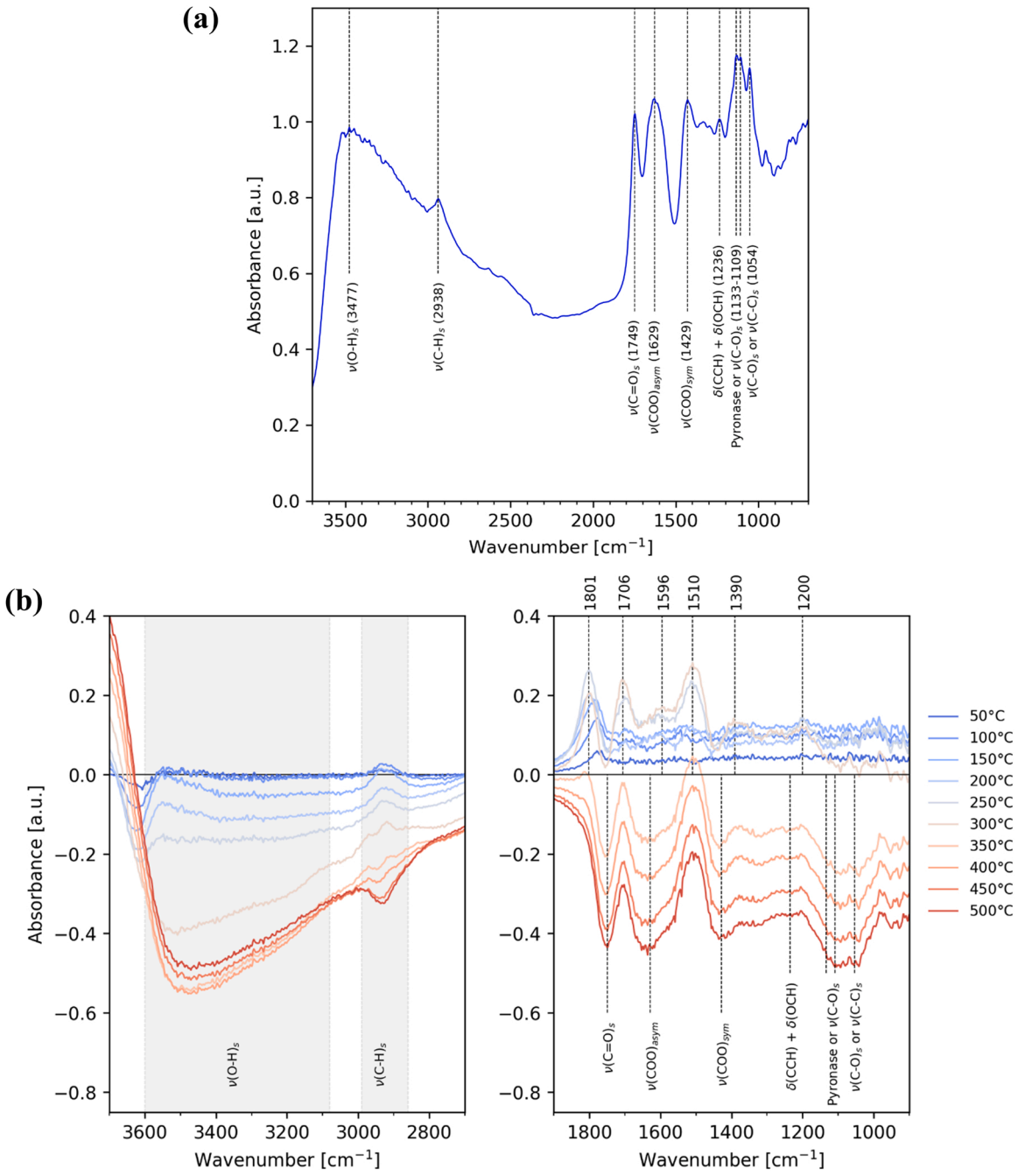

Fig. 9. DRIFTS measurements of pyrolysis of Fe-Alginate from RT to 500 °C. a) The absorbance of Fe-Alginate at RT, b) The absorbance was calculated using the RT measurement as I_0, and subsequent measurements as I, where positive and negative values imply an increase and decrease in absorbance relative to Fe-alginate, respectively, and the wavenumbers listed above the figure correspond to bands emerging during the pyrolysis.

single-beam data of the sample measured at RT °C as I_0, to visualize the change towards 500 °C (Fig. 9(b)), while the raw single-beam data can be found in Supporting information (Fig. S18). The reduction of the wide $\nu(O\text{-}H)_s$ band shows that water was gradually removed with increasing temperature, but the shoulder at 3480 cm^{-1} persisted until 200 °C. The position of this shoulder indicates intermolecularly bonded hydroxyl groups, perhaps linked to Fe-species, but it ultimately diminished when transitioning to 300 °C. The absorbance in the O-H region dropped severely from 250 to 350 °C. The absorbance of $\nu(C\text{-}H)_s$ increased initially, but was diminished at 350 °C and appeared to be removed as the temperature reached 450 °C, at which point the signal deteriorated rapidly.

In the region of 1800–1000 cm^{-1}, the overall absorbance increased initially but reduced with increasing temperature after 150 °C. The most dramatic loss of overall absorbance was observed between 300 °C and 350 °C, affecting the entire region. A band appeared at 1767 cm^{-1} at 50 °C, accompanied by a gradually increasing band at 1801 cm^{-1}. We assign the bands at 1767 cm^{-1} and 1801 cm^{-1} to the formation of an acid anhydride, where the peaks correspond to the symmetric and asymmetric stretching vibrations of the carbonyl groups, respectively. The higher intensity observed for the asymmetric peak indicates that the acid anhydride forms intermolecular bonds between the alginate chains, via the association of two carboxylate groups [42].

The $\nu(C{=}O)_s$ at 1749 cm^{-1} and $\nu(COO)_{sym}$ were the first bands in this region to decrease in absorbance, between 200 and 250 °C. Simultaneously, new bands appeared at 1706 cm^{-1} and 1596 cm^{-1}, and 1510 cm^{-1}. The band at 1596 cm^{-1}, which we assign to $\nu(C{=}C)_s$, was removed by 350 °C and appears to be an intermediate structure. The change for $\nu(COO)_{asym}$ is difficult to assess precisely due to overlapping bands. The bands at 1510 cm^{-1} and 1706 cm^{-1} have frequencies that indicate $\nu(C{=}C)_{s,skeletal}$ and $\nu(C{=}O)_s$, respectively [43,44], and they persisted throughout the investigated temperature range. There were also bands emerging at 1390 and 1200 cm^{-1}, in the region where O-H bending and C-O stretching is typically located.

4. Discussion

4.1. The Fe-alginate structure

The Fe^{3+} introduced during the synthesis step was also observed when characterizing the dried Fe-alginate. Distinguishing the interaction between alginate and Fe^{3+} requires a powerful tool that may investigate the local alginate structure, such as nuclear-magnetic resonance (NMR). Unfortunately, the paramagnetism of the iron species makes high-resolution NMR unfeasible. The interaction of divalent transition metals with alginate is well-studied, but these results do not translate for trivalent cations. Not only is the binding strength between alginate and trivalent cations much higher than for the divalent cations, but the ionic radii are also of importance - a smaller ionic radius allows for tighter intermolecular interactions between the alginate macromolecules. Investigations of Al^{3+}-alginate by NMR showed two different octahedral six-fold coordination sites [45]. The Fe^{3+} ion is slightly larger than Al^{3+}, but similarities in binding mode can be expected. In our previous work, Fe^{3+}-alginate was compared to alginates cross-linked with divalent cations, where the latter had more distinct $\nu(COO)_{asym}$ and $\nu(COO)_{sym}$ than Fe^{3+}-alginate [41]. An EXAFS measurement was performed of Fe-alginate at RT (Table S4, Fig. S15), which indicated that the Fe atoms on average were coordinated with 6 oxygens. However, the oxygen can stem from both carboxyl and hydroxyl groups, and it is also difficult to differentiate light scatterers such as oxygen and carbon.

4.2. Evolution of the pyrolysis process

During pyrolysis, the fate of the iron and alginate was linked, due to their initial interaction in Fe-alginate. At first, water was removed by drying as seen from the first mass-loss segment in TGA, but the iron species appeared unchanged. The reduction of Fe^{3+} to Fe^{2+} took place between 150 and 200 °C without involving the common reduction route through γ-Fe_3O_4. Instead, a direct reduction to Fe^{2+} was observed, seemingly while still bound to alginate. The reduction of Fe^{3+} liberated some carboxyl groups and might have resulted in the formation of intermolecular bonded acid anhydride. This was the beginning of the largest mass-loss (50 %) segment in TGA that started at 160 °C, and lasted up to 350 °C, encompassing H_2O formation due to loss of hydroxyl groups and possibly also due to dehydration during the development of acid anhydrides and freeing up of carboxylates. The formation of FeO occurred in the range of 200–400 °C, which further destabilized the carboxyl groups, and possibly also hydroxyl groups, but crystallites with sufficient ordering were observed at 380 °C. This mass-loss was also observed for divalent metals in the same temperature range [41]. New C═C and C═O double bonds were also formed, while the bands related to the pyranose rings were severely reduced by 400 °C, implying that the ring structures of the monomers are fractured or transformed, which is consistent with the third mass-loss (11 %) segment.

The carbon structure was further investigated by observing the D-band and G-band, which indicated that the carbon support carbonized by removing heteroatoms and formation of small carbon subunits up to 700 °C. Above 630 °C, the extent of carbonization appears to be sufficient to let carbon act as a reductant, as FeO was rapidly reduced to Fe, releasing CO and CO_2 that resulted in a mass-loss of 11 %. Our previous investigations of the pyrolysis of metal-alginates with Fe, Co, Ni, and Cu, showed that Fe-Alginate was the only sample to have a mass loss in TGA after 550 °C, accompanied by CO and CO_2 loss. The in situ XRD showed only clear diffractions of α-Fe, while both Mössbauer and XRD of the passivated P700 sample indicated that θ-Fe_3C was also formed. Differentiating α-Fe to θ-Fe_3C with XANES is not straightforward, but its absence during in situ XRD could be due to the low ordering of the Fe_xC/θ-Fe_3C and might require dwelling at 700 °C to develop.

4.3. The effect of pyrolysis temperature on the catalytic properties

Analysis of the spent samples indicated that the Fe-alginate sample pyrolyzed at 700 °C was carburized to a greater extent and was able to activate more iron particles than those treated at lower temperatures. Yet, the samples pyrolyzed at low temperatures yielded the highest catalytic activity. A correlation was observed between catalytic activity at the end of FTS experiment and the average particle size in the spent sample (Fig. S10) – the sample pyrolyzed at 400 °C achieved noticeably lower Fe loading (20 %) than the others (27–33 %), due to less decomposition of the support. This was beneficial, as low metal loading reduced the proximity of the metal particles, effectively lowering the extent of sintering.

All catalysts exhibited the same iron phases during reaction, although with different compositions. The active phase during reaction is χ-Fe_5C_2, but having a higher extent of carburization did not seem to be beneficial – the greater extent of carburization for P700 did not yield higher activity. The catalytic stability of P700 seemed to be the best due to the sample having relatively large particles before reduction and reaction, and therefore the loss of catalytic activity due to sintering was limited. The in situ FTS measurement of the sample pyrolyzed at 500 °C indicated that the sample consisted of 18 % χ-Fe_5C_2 after 20 h of FTS. Thus, the relatively small amount of the total iron that is carburized and responsible for the catalytic activity of P500 must be highly dispersed. Sintering should be limited to maintain the activity, as it appears to be the main cause of deactivation.

While there were no apparent differences in olefin selectivity, more short-chain hydrocarbons were produced by the catalysts pyrolyzed at lower temperatures. All samples had the same amount of Na and S relative to Fe, but higher pyrolysis temperatures could potentially increase the segregation of sulfur to the surface of the Fe particles, but due to the low amount of S, it could not be quantified by XPS. Relative to the previous study (0.13 wt% Na and 0.19 wt% S) on this type of catalyst, a

more efficient washing procedure was employed, which lowered the Na content to 0.05 wt% and reduced the C_2-C_4 olefin/paraffin (O/P) ratio from 2.0 to 1.0 [28]. The selectivity of C_2-C_4 olefins could therefore be improved by the addition of Na by incipient wetness impregnation. For this type of study, it is important to take into consideration that the Na and S originating from the precursor in the synthesis step are distributed differently in the material than if it is added to the pores of the support by impregnation.

All the treatments performed on Fe-alginate resulted in materials with desirable catalytic properties, as the events that led to the decomposition of the alginate structure and initiated the carbonization took place around 400 °C. P400 obtained the most desirable catalytic properties for FTS, with high activity and without significant changes in hydrocarbon selectivity.

5. Conclusion

The pyrolysis process of Fe-Alginate to form carbon-supported iron catalysts was investigated. The in situ characterization revealed that the Fe^{3+} species in alginate reduce to Fe^{2+} around 180 °C, at the same time as the alginate starts to restructure and decompose. The formation of FeO crystallites led to the loss of carboxyl and hydroxyl groups, and new C═C and C═O bonds in the alginate residues. At temperatures exceeding 630 °C, a complete reduction to α-Fe took place, where the carbon in the support acts as a reductant, with the observed release of CO and CO_2. The resulting carbon support is formed by the deterioration of the alginate, and the most critical events that aid the formation of a catalyst with desirable properties took place at temperatures up to 400 °C. The results provide valuable knowledge to the rational design of metal-alginate-based materials with tailored structures and properties for various applications.

Catalysts were synthesized by performing pyrolysis at temperatures between 400 and 700 °C, all of which resulted in appreciable material characteristics for heterogeneous catalysts. With increasing pyrolysis temperature, the particle size increased, as well as the reductive nature of the treatment, and a larger surface area but smaller pores were formed. All the catalysts exhibited great performance in high-temperature FTS, but higher catalytic activity was observed for catalysts synthesized at milder temperatures due to restricted alginate mass-loss. This resulted in lower Fe loading, which limited particle growth and had a beneficial effect on the catalytic surface area and activity. A greater extent of carburization during FTS was observed for the sample pyrolyzed at 700 °C, but this did not enhance the catalytic activity nor selectivity to a significant extent.

CRediT authorship contribution statement

Joakim Tafjord: Conceptualization, Methodology, Validation, Software, Formal analysis, Investigation, Resources, Data curation, Writing – original draft, Writing – review & editing, Visualization. **Samuel K. Regli**: Methodology, Software, Formal analysis, Investigation, Writing – review & editing. **Achim Iulian Dugulan:** Methodology, Formal analysis, Investigation, Data curation, Writing – review & editing. **Magnus Rønning**: Investigation, Resources, Supervision, Writing – review & editing. **Erling Rytter:** Conceptualization, Writing – review & editing. **Anders Holmen:** Conceptualization, Writing – review & editing. **Rune Myrstad:** Resources, Writing – review & editing. **Jia Yang:** Conceptualization, Investigation, Resources, Writing – original draft, Writing – review & editing, Supervision, Project administration, Funding acquisition.

Author Contributions

The manuscript was written through the contributions of all authors. All authors have approved the final version of the manuscript.

Declaration of Competing Interest

The authors declare that they have no known competing financial interests or personal relationships that could have appeared to influence the work reported in this paper.

Data Availability

Data will be made available on request.

Acknowledgements

The authors would like to acknowledge support from the Research Council of Norway through the Norwegian Center for Transmission Electron Microscopy, NORTEM (197405/F50); the iCSI (industrial Catalysis Science and Innovation) Centre for Research-based Innovation (Contract no. 237922); and the Swiss-Norwegian Beamlines at ESRF (Grant no. 296087). Funding from the Norwegian University of Science and Technology (NTNU) is also acknowledged. The assistance of Ljubisa Gavrilovic and the staff at the Swiss-Norwegian Beamlines at ESRF during the synchrotron beam-time is also acknowledged.

Appendix A. Supporting information

Supplementary data associated with this article can be found in the online version at doi:10.1016/j.apcata.2022.118834.

References

[1] S.K. Tiwari, V. Kumar, A. Huczko, R. Oraon, A.D. Adhikari, G.C. Nayak, Crit. Rev. Solid State Mater. Sci. 41 (4) (2016) 257–317, https://doi.org/10.1080/10408436.2015.1127206.
[2] S. Dong, X. He, H. Zhang, X. Xie, M. Yu, C. Yu, N. Xiao, J. Qiu, J. Mater. Chem. A 6 (33) (2018) 15954–15960, https://doi.org/10.1039/C8TA04080J.
[3] P.-y. Hung, K.-t. Lau, B. Fox, N. Hameed, J.H. Lee, D. Hui, Compos. Part B: Eng. 133 (2018) 240–257, https://doi.org/10.1016/j.compositesb.2017.09.010.
[4] J. Tang, W. Zhu, R. Kookana, A. Katayama, J. Biosci. Bioeng. 116 (6) (2013) 653–659, https://doi.org/10.1016/j.jbiosc.2013.05.035.
[5] M. Keiluweit, P.S. Nico, M.G. Johnson, M. Kleber, Environ. Sci. Technol. 44 (4) (2010) 1247–1253, https://doi.org/10.1021/es9031419.
[6] D.W. Wang, F. Li, M. Liu, G.Q. Lu, H.M. Cheng, Angew. Chem. Int. Ed. Engl. 47 (2) (2008) 373–376, https://doi.org/10.1002/anie.200702721.
[7] Y. Yang, K. Chiang, N. Burke, Catal. Today 178 (1) (2011) 197–205, https://doi.org/10.1016/j.cattod.2011.08.028.
[8] B. Liu, H. Shioyama, T. Akita, Q. Xu, J. Am. Chem. Soc. 130 (16) (2008) 5390–5391, https://doi.org/10.1021/ja7106146.
[9] Y. Ding, B. Jin, G. Gu, X.-H. Xia, J. Mater. Chem. 19 (48) (2009) 9141–9146, https://doi.org/10.1039/B913767J.
[10] A. Martinsen, G. Skjåk-Bræk, O. Smidsrød, Biotechnol. Bioeng. 33 (1) (1989) 79–89.
[11] Y. Liu, J.-S. Wang, P. Zhu, J.-C. Zhao, C.-J. Zhang, Y. Guo, L. Cui, J. Anal. Appl. Pyrolysis 119 (2016) 87–96, https://doi.org/10.1016/j.jaap.2016.03.014.
[12] Y. Liu, J.-C. Zhao, C.-J. Zhang, Y. Guo, L. Cui, P. Zhu, D.-Y. Wang, RSC Adv. 5 (79) (2015) 64125–64137, https://doi.org/10.1039/c5ra11048c.
[13] Y. Liu, C.J. Zhang, J.C. Zhao, Y. Guo, P. Zhu, D.Y. Wang, Carbohydr. Polym. 139 (2016) 106–114, https://doi.org/10.1016/j.carbpol.2015.12.044.
[14] Y. Liu, J.-C. Zhao, C.-J. Zhang, Y. Guo, P. Zhu, D.-Y. Wang, J. Mater. Sci. 51 (2) (2016) 1052–1065, https://doi.org/10.1007/s10853-015-9435-9.
[15] Y. Liu, X.-R. Zhao, Y.-L. Peng, D. Wang, L. Yang, H. Peng, P. Zhu, D.-Y. Wang, Polym. Degrad. Stab. 127 (2016) 20–31, https://doi.org/10.1016/j.polymdegradstab.2015.12.024.
[16] J.S. Rowbotham, P.W. Dyer, H.C. Greenwell, D. Selby, M.K. Theodorou, Interface Focus 3 (1) (2013) 20120046, https://doi.org/10.1098/rsfs.2012.0046.
[17] J. Zhang, Q. Ji, F. Wang, L. Tan, Y. Xia, Polym. Degrad. Stab. 97 (6) (2012) 1034–1040, https://doi.org/10.1016/j.polymdegradstab.2012.03.004.
[18] A.A. Said, Polym. Degrad. Stab. 39 (1993) 393–397.
[19] J. Wu, H. Zheng, F. Zhang, R.J. Zeng, B. Xing, Chem. Eng. J. 362 (2019) 21–29, https://doi.org/10.1016/j.cej.2019.01.009.
[20] Y. Li, M. Zhou, G.I.N. Waterhouse, J. Sun, W. Shi, S. Ai, Environ. Sci. Pollut. Res. 28 (5) (2021) 5149–5157, https://doi.org/10.1007/s11356-020-10859-0.
[21] C. Lei, Y. Song, F. Meng, Y. Sun, D.C.W. Tsang, K. Yang, D. Lin, Sci. Total Environ. 756 (2021), 143866, https://doi.org/10.1016/j.scitotenv.2020.143866.
[22] M. Latorre-Sanchez, A. Primo, H. Garcia, J. Mater. Chem. 22 (40) (2012), https://doi.org/10.1039/c2jm34978g.
[23] D. Li, D. Yang, X. Zhu, D. Jing, Y. Xia, Q. Ji, R. Cai, H. Li, Y. Che, J. Mater. Chem. A 2 (44) (2014) 18761–18766, https://doi.org/10.1039/C4TA03052D.

[24] W. Chen, M. Luo, K. Yang, X. Zhou, Int. J. Biol. Macromol. 158 (2020) 265–274, https://doi.org/10.1016/j.ijbiomac.2020.04.123.
[25] L. Zhang, T. Liu, N. Chen, Y. Jia, R. Cai, W. Theis, X. Yang, Y. Xia, D. Yang, X. Yao, J. Mater. Chem. A 6 (38) (2018) 18417–18425, https://doi.org/10.1039/C8TA07469K.
[26] A. Primo, J. He, B. Jurca, B. Cojocaru, C. Bucur, V.I. Parvulescu, H. Garcia, Appl. Catal. B: Environ. 245 (2019) 351–359, https://doi.org/10.1016/j.apcatb.2018.12.034.
[27] S.K. Papageorgiou, E.P. Favvas, A.A. Sapalidis, G.E. Romanos, F.K. Katsaros, J. Hazard. Mater. 189 (1–2) (2011) 384–390.
[28] J. Tafjord, E. Rytter, A. Holmen, R. Myrstad, I.-H. Svenum, B.E. Christensen, J. Yang, ACS Appl. Nano Mater. 4 (4) (2021) 3900–3910, https://doi.org/10.1021/acsanm.1c00294.
[29] Z. Klencsár, Nucl. Instrum. Methods Phys. Res. Sect. B: Beam Interact. Mater. At. 129 (4) (1997) 527–533, https://doi.org/10.1016/S0168-583X(97)00314-5.
[30] T.A. Wezendonk, V.P. Santos, M.A. Nasalevich, Q.S. Warringa, A.I. Dugulan, A. Chojecki, A.C. Koeken, M. Ruitenbeek, G. Meima, H.-U. Islam, G. Sankar, M. Makkee, F. Kapteijn, J. Gascon, ACS Catal. 6 (5) (2016) 3236–3247.
[31] M. Rønning, N.E. Tsakoumis, A. Voronov, R.E. Johnsen, P. Norby, W. van Beek, Ø. Borg, E. Rytter, A. Holmen, Catal. Today 155 (3) (2010) 289–295, https://doi.org/10.1016/j.cattod.2009.10.010.
[32] W. Windig, J. Guilment, Anal. Chem. 63 (14) (1991) 1425–1432.
[33] A. Martini, E. Borfecchia, Crystals 10 (8) (2020) 664.
[34] S. Bernard, O. Beyssac, K. Benzerara, N. Findling, G. Tzvetkov, G.E. Brown, Carbon 48 (9) (2010) 2506–2516, https://doi.org/10.1016/j.carbon.2010.03.024.
[35] D.B. Schuepfer, F. Badaczewski, J.M. Guerra-Castro, D.M. Hofmann, C. Heiliger, B. Smarsly, P.J. Klar, Carbon 161 (2020) 359–372, https://doi.org/10.1016/j.carbon.2019.12.094.
[36] Y. Cheng, J. Lin, K. Xu, H. Wang, X. Yao, Y. Pei, S. Yan, M. Qiao, B. Zong, ACS Catal. 6 (1) (2016) 389–399, https://doi.org/10.1021/acscatal.5b02024.
[37] B. An, K. Cheng, C. Wang, Y. Wang, W. Lin, ACS Catal. 6 (6) (2016) 3610–3618, https://doi.org/10.1021/acscatal.6b00464.
[38] Y. Wei, D. Luo, L. Yan, J. Liu, Q. Cheng, M. Cai, S. Sun, X. Wen, Y. Yang, C. Zhang, Energy Fuels 35 (5) (2021) 4428–4436, https://doi.org/10.1021/acs.energyfuels.1c00168.
[39] Z. Schnepp, S.C. Wimbush, M. Antonietti, C. Giordano, Chem. Mater. 22 (18) (2010) 5340–5344, https://doi.org/10.1021/cm101746z.
[40] L. Li, Y. Fang, R. Vreeker, I. Appelqvist, E. Mendes, Biomacromolecules 8 (2) (2007) 464–468, https://doi.org/10.1021/bm060550a.
[41] J. Tafjord, E. Rytter, A. Holmen, R. Myrstad, I.-H. Svenum, B.E. Christensen, J. Yang, ACS Appl. Nano Mater. (2021), https://doi.org/10.1021/acsanm.1c00294.
[42] S.-Y. Lin, H.-L. Yu, M.-J. Li, Polymer 40 (12) (1999) 3589–3593, https://doi.org/10.1016/S0032-3861(98)00488-1.
[43] H. Düdder, A. Wütscher, R. Stoll, M. Muhler, Fuel 171 (2016) 54–58, https://doi.org/10.1016/j.fuel.2015.12.031.
[44] M. Poletto, A.J. Zattera, R.M.C. Santana, J. Appl. Polym. Sci. 126 (S1) (2012) E337–E344, https://doi.org/10.1002/app.36991.
[45] J. Brus, M. Urbanova, J. Czernek, M. Pavelkova, K. Kubova, J. Vyslouzil, S. Abbrent, R. Konefal, J. Horský, D. Vetchy, J. Vysloužil, P. Kulich, Biomacromolecules 18 (8) (2017) 2478–2488, https://doi.org/10.1021/acs.biomac.7b00627.